Document downloaded from:

http://hdl.handle.net/10251/198241

This paper must be cited as:

Galindo, J.; Navarro, R.; Tarí, D.; Moya, F. (2022). Quantitative validation of an in-flow water condensation model for 3D-CFD simulations of three-way junctions using indirect condensation measurements. International Journal of Thermal Sciences. 172(107303):1-11. https://doi.org/10.1016/j.ijthermalsci.2021.107303

The final publication is available at

https://doi.org/10.1016/j.ijthermalsci.2021.107303

Copyright Elsevier

Additional Information

NOTICE:

this is the author's version of a work that was accepted for publication in International Journal of Thermal Sciences. Changes resulting from the publishing process, such as peer review, editing, corrections, structural formatting, and other quality control mechanisms may not be reflected in this document. Changes may have been made to this work since it was submitted for publication. A definitive version was subsequently published as [1]:

References

[1] J. Galindo, R. Navarro, D. Tari, F. Moya, Quantitative validation of an inflow water condensation model for 3D-CFD simulations of three-way junctions using indirect condensation measurements, International Journal of Thermal Sciences 172 (2022) 1–11. doi:10.1016/j.ijthermalsci.2021.107303.

Quantitative validation of an in-flow water condensation model for 3D-CFD simulations of three-way junctions using indirect condensation measurements.

J. Galindo[a], R. Navarro[a], D. Tarí[a], F. Moya[a,*]

[a] *CMT - Motores Térmicos, Universitat Politècnica de València*
Camino de Vera, 46022 Valencia

Abstract

The usage of three way junctions to merge fluid streams is widely extended. For certain applications, such as refrigeration systems or internal combustion engines, the mixing of humid gaseous flow leads to bulk condensation, which compromises the integrity of the downstream elements. In this work, a test bench is adapted to manage the mixing of wet streams and a novel experimental technique is developed to measure condensation indirectly. Well-resolved temperature distributions are measured by means of a rotating array of thermocouples at experiments with and without humidity. Enthalpy balances using temperature distributions of both cases allow to infer the condensation mass fraction field. 3D CFD simulations with an in-flow condensation sub-model are compared with these measurements for two junction geometries and two operating conditions, with an average agreement of 11% in terms of condensation mass flow rate. The three-way junction design and its ability to reduce mixing is found to be of paramount importance to reduce bulk condensation. This validated model is therefore suitable for optimizing the junction geometry in terms of condensation reduction. With limited water condensation, NO_x, CO_2 and particulate matter emissions can be strongly abated for internal combustion engines by extending the usage of low-pressure exhaust gas recirculation to cold conditions.

Keywords: Condensation measurements, Computational Fluid Dynamics, Mixing streams, Model validation, Low-Pressure EGR, Enthalpy balance

1. Introduction

The situation of fluid streams that need to be blended appears in many fields of application, including oil industry [1], power plants [2, 3, 4], internal combustion engines [5, 6] and refrigeration systems [7], amongst others. The characteristics of the mixing process can be of paramount importance in some scopes. For instance, blending subsaturated streams of different psychrometric conditions can lead to condensation at the mixing chamber of air handling units [8] or at internal combustion engine junctions [9].

This work investigates experimentally and with 3D CFD simulations the mixing of humid streams in a junction at situations that lead to condensation. The produced condensation is particularly harmful for the case of exhaust gases mixing with cold ambient air in a turbocharged internal combustion engine working with Low-Pressure Exhaust Gas Recirculation (LP-EGR) [9]. In this case, water droplets may reach the compressor impeller and cause wear on the surface [10, 11, 12]. LP-EGR is a promising technology due to its high potential on reducing NO_x, CO_2 and particulate matter emissions [13]. However, the critical drawback of the generation of condensates not only in the LP-EGR junction but also at the LP-EGR cooler [14, 15, 16] has challenged researchers to address this issue.

There is a large body of research on flow mixing phenomena at three-way junctions. Some researchers, like Georgiou et

*Corresponding author. Tel.: +34 963 877 650
Email addresses: galindo@mot.upv.es (J. Galindo), ronagar1@mot.upv.es (R. Navarro), datade@mot.upv.es (D. Tarí), framoto1@mot.upv.es (F. Moya)

al. [17] and Sakowitz et al. [18], have focused their studies on modeling issues of turbulent flow mixing in T-junctions. Thermal mixing has gained the attention of authors like Evrim et al. [19, 20, 21], Zhou et al. [22, 23] or Bornschlegell et al. [24]. The impact of mixing in LP-EGR junctions on compressor performance has been already assessed [25, 26, 27]. Unfortunately, all these previous works consider single-phase fluids. Yang et al. [28] conducted a literature review about T-junctions for phase separation, which considers one stream and splits it into two streams, contrarily to flow mixing (two inlets and a single outlet). Therefore, condensation does not play a role in phase separation problems. Despite the vast literature available on junction flow, the conducted review shows a lack of insight into condensation phenomena due to the mixing process in three-way junctions.

In the past years, some advancements have been made in this topic. To study the condensation generation at mixing processes, Serrano et al. [29] proposed an in-flow water condensation model to be embedded in 3D-CFD codes. Galindo et al. [30] confirmed that this CFD model provides good agreement against measurements in terms of secondary flows and shape of condensation patterns, considering the latter as a proof of qualitative validation in the scope of in-flow condensation. The usefulness of the model was evinced by Galindo et al. [31], which compared the experimental results of impeller durability tests with 3D-CFD simulations, showing that higher predicted condensation rates corresponded to stronger impeller erosion. In this way, the condensation mass flow rate is the *figure of merit* of the junction that should be minimized to limit compressor damage. It seems therefore convenient to assess how junction design and operating conditions dictate the generated condensation mass flow rate. Unfortunately, the prediction of condensation by means of 3D CFD simulations has not been quantitatively validated yet.

Instead, if the quantification of in-flow condensation mass flow rate is addressed experimentally, several issues arise. Some authors like Wang et al. [32] proposed an H_2O absorption tomography to quantify in-flow water vapor on a Diesel Particle Filter. However, this technique provides H_2O vapor mole fraction instead of the desired liquid water mass flow rate. A method to collect liquid water (after humid air has been externally cooled in a heat exchanger) and measure its mass flow rate is the usage of separators ([33, 34]). This technique is not valid in the framework of junction condensation, as the vortical flow established in such devices promote flow mixing ([35, 36]) and thus will spuriously increase the generated condensation [9]. Therefore, no adequate experimental quantification of junction condensation mass flow rate has been found in the literature, and in turn 3D CFD models designed to predict condensation cannot be validated.

To overcome these challenges, an innovative technique is developed in this work to conduct an indirect measurement of the bulk flow water condensation rate, based on an enthalpy balance on the cross section of study. This technique takes advantage of the energy released (latent heat) of the condensation process in order to infer the condensation rate, through finely-resolved campaigns of temperature measurements with and without formation of condensation. The main novelty of this research is therefore the development of a method for experimentally quantifying the condensation produced by mixing streams, which required a non-intrusive approach that preserved the flow pattern. In this paper, experimental and numerical condensation rate distributions (together with generated mass flow rates of condensates) at junction outlets are therefore provided and compared for the first time. The experimental technique can be then employed as a stand-alone tool, to help developing junction designs with reduced generated condensation; or to validate 3D-CFD condensation models used for the same purpose.

In Section 2 the experimental test bench and instrumentation is described. Next, in section 3, the numerical configuration of the CFD simulations conducted with STAR-CCM+ [37] is explained, together with the condensation submodel employed. The methodology to characterize the in-flow water condensation through temperature measurements is derived in Section 4. The results are presented and discussed in Section 5,

comparing 3D CFD simulations and experiments in terms of temperature and condensation distributions for two junctions geometries and two different operating points. Particularly, the calculation of the total water mass flow rate going through a given section is employed to quantitatively validate the 3D CFD configuration. Finally, the conclusions obtained from the usage of the developed technique and the validation of the 3D CFD condensation model are exposed in Section 6.

2. Experimental setup and methodology

In this section, a description of the test bench facility, including the different systems used, is shown. Experiments were carried out in a continuous humid flow test rig. The temperature array installed at the outlet cross section is described with details, since it is the key factor to be able to perform the indirect measurement of water condensation.

2.1. Experimental facility

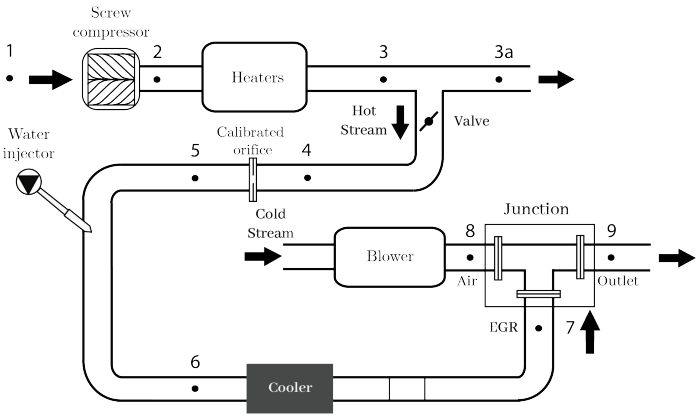

Figure 1: Scheme of the humid flow test rig employed.

A humid flow test rig is designed to supply the three-way junction with two streams of moist air at the required psychrometric conditions, in order for them to be mixed at the junction and in this way produce in-flow condensation. A scheme of the test rig is depicted in Fig. 1. For LP-EGR applications, the stream of hot humid flow (station 7) would represent the EGR flow and the stream of cold flow (station 8) would represent the fresh air coming from the ambient during cold conditions.

In the branch devoted to produce hot stream (EGR line), a screw compressor located between stations 1 and 2 drives the flow, and a set of five heaters (45kW in total) is used to increase the flow temperature. Then, a calibrated orifice allows to set the target mass flow rate (MFR) by controlling the pressure drop between stations 4 and 5 (see Fig. 1). A water injector is used to increase the specific humidity of the hot stream to the target. Target flow temperature at the three-way junction "EGR" inlet (station 7) is achieved by means of a water-cooled heat exchanger (cooler). Regarding the cold flow branch, a blower drives the flow from a climatic chamber to the three-way junction "air" inlet (station 8). The blower rotational speed and the climatic chamber temperature are controlled in order to obtain the desired conditions at station 8. In order to guarantee a homogeneous flow in stations 7 and 8 (inlet legs of the three-way junction), the last stage of their connections is performed by straight ducts with lengths greater than 10 corresponding diameters.

Table 1 shows the characteristics of the instrumentation employed at the test rig with its accuracy. K-type thermocouples are used for measuring temperature at all flow test rig stations as well as in the temperature array placed at the junction outlet (see Fig. 2). Piezoresistive pressure sensor are installed at different stations, particularly at the calibrated orifice inlet and outlet to set the hot stream mass flow rate. A weighing scale is used in the water injector to check that the system is injecting the desired amount of water mass flow in the EGR line. The cold flow branch presents a flow meter, while the frequency control of the blower allows to establish the corresponding MFR.

2.2. Temperature array measurement

Figure 2 depicts the array of thermocouples set in the three-way junction outlet (station 9 in Fig. 1), in order to characterize the temperature distribution in the cross section of study. Table 2 shows the reference locations of the 5 thermocouples, which are set at different radial and circumferential positions. The ability of the array to be rotated azimuthally along the 360° allows the thermocouples to characterize the whole cross-

Sensor	Variable	Range	Accuracy [%]
Thermocouples K-type	Temperature	-260 – 1260 °C	1
Pressure sensor	Pressure	0 – 6 bar	0.3
Flow meter	Air mass flow	0 – 720 kg/h	1
Weighing scale	Water injected mass	0 – 20 kg	0.1

[1] According to datasheets

Table 1: Instrumentation range and accuracy[1]

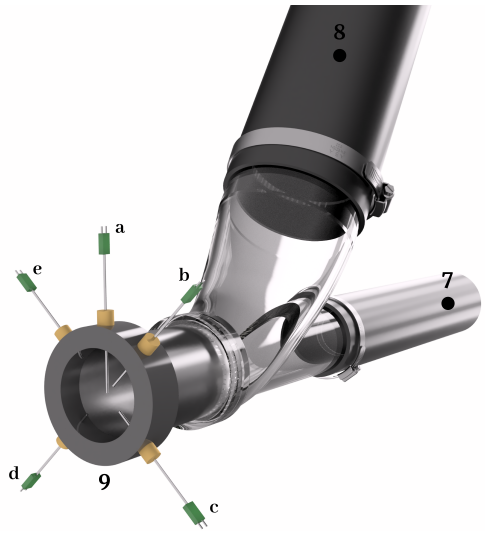

Figure 2: Representation of the thermocouple array located at the junction outlet section.

	a	b	c	d	e
Protrusion	R	0.75R	0.5R	0.25R	1 mm
θ (angle)	0°	45°	135°	225°	315°

Table 2: Thermocouple array protrusion and angle

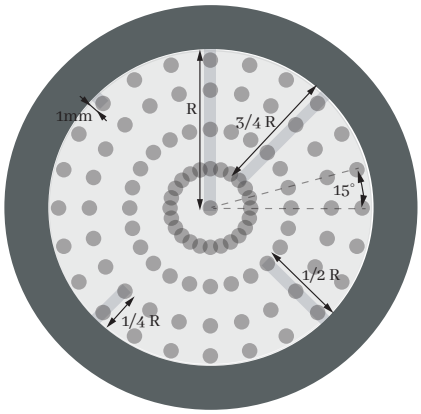

Figure 3: Location of 97 temperature measurements performed at the juntion outlet section.

section. Measurements were taken at 24 different angular positions of the thermocouple array, each of them shifted by 15°, resulting in a total of 97 temperature measurements evenly distributed in the cross section as depicted in Fig. 3. Test repeatability was ensured by checking that the temperatures were consistent with the initial readings after a whole rotation (360°). For easier processing and visualization of the results shown in sections 4 and 5, a linear interpolation of the temperature will be performed between the points. The annulus consisting in the outer area between the thermocouple "e" (see Fig. 2 and Table 2) and the wall is not being extrapolated or displayed in the images, but it will be considered for the calculation of condensation mass flow rate in order to compare with the 3D CFD simulations across the whole cross section.

3. Numerical configuration

In this section, a description of the CFD model domain, mesh, setup and condensation submodel is provided. The numerical configuration is based on the works of Galindo et al. [9, 31].

3.1. Geometry and mesh

The region of interest is a three-way junction, where EGR (humid and warm flow) is mixed with the main inlet stream (at cold conditions), as seen in Figure 4. Extrusions of three diameters at both inlets and five additional diameters at the outlet are

set, assuring that the location of the boundaries is not affecting the solution at the region of interest (junction). A sensitivity analysis of the intake extrusions length was conducted, showing that increasing the extrusions inlets up to 5 diameters made a difference on condensation at the cross-section of study of only 0.7 %. However, removing the extrusion diameters caused a change of 5 % on condensation. Therefore, 3-diameters-long extrusions were employed at the inlet and EGR boundaries for the sake of computational cost.

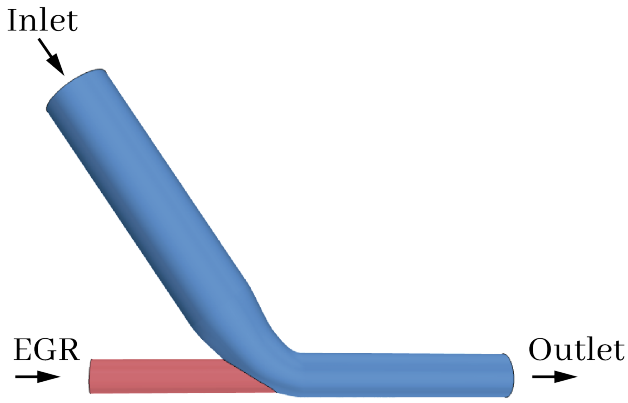

Figure 4: Complete geometry of the LP-EGR junction

The meshes are composed of 3 million polyhedral cells with a base size of 0.6 mm. Figure 5 depicts the grids for both geometries that will be employed in the simulation campaign described in Section 4.2. In the extruded regions, the corresponding cross section mesh is swept longitudinally. Eight prism layers are created in the vicinity of the walls in order to improve the prediction of the boundary layer. A grid independence study was performed at point P1wet (see Table 3) considering the geometry of Fig. 5a (since it provides stronger secondary flows and mixing) with three different cell accounts: 300 thousand, 3 and 11 million elements. Figures 6 and 7 show respectively the profiles of temperature and condensed water mass fraction at the vertical diameter of the junction outlet, which is represented as a solid line in Fig. 5. The distributions plotted in Figs. 6 and 7 are in great agreement for the grids of 3M and 11M cells, whereas the mesh of 300k elements provides dissimilar profiles. In this way, the refinement from 300k to 3M cells changed condensation predicted by 13%, but a difference of only 1% was observed for the increase between 3 to 11 million cells. To limit the computational effort, the mesh of 3 million elements was therefore selected for the whole numerical campaign. This grid provides 99% of its wall cells below a y^+ of 1.

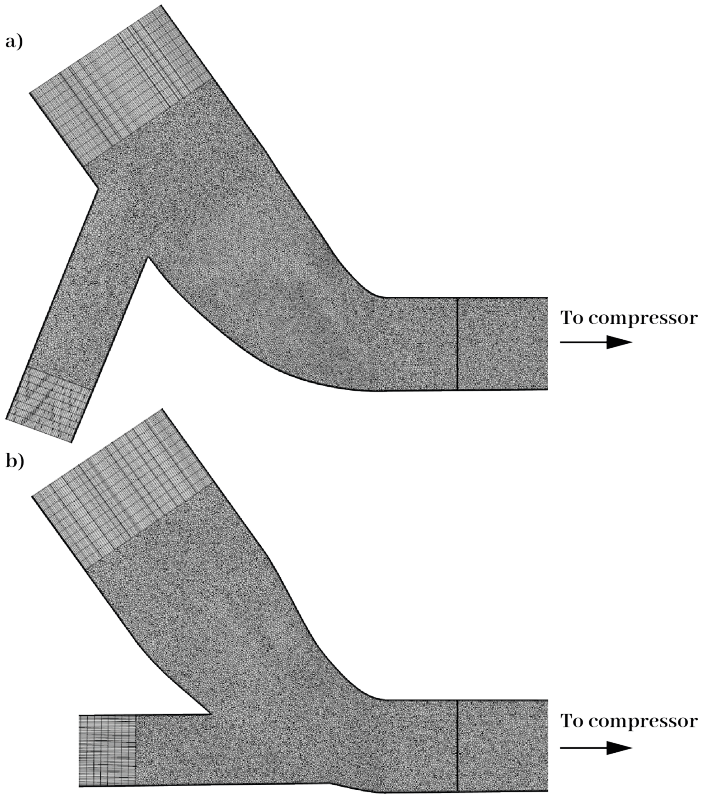

Figure 5: High-mixing (above) and low-mixing (below) three-way junctions studied, with longitudinal section of mesh.

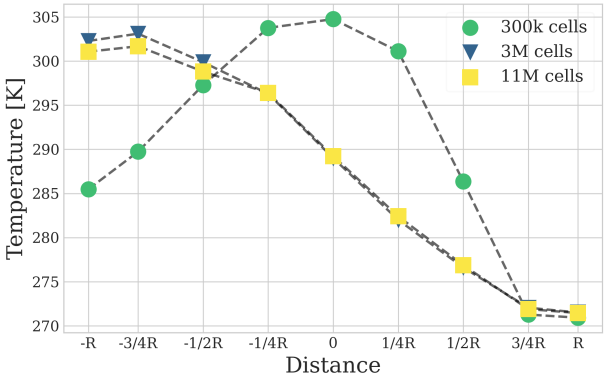

Figure 6: Temperature profiles for different grid densities at vertical diameter of high-mixing junction outlet at the operating point P1wet.

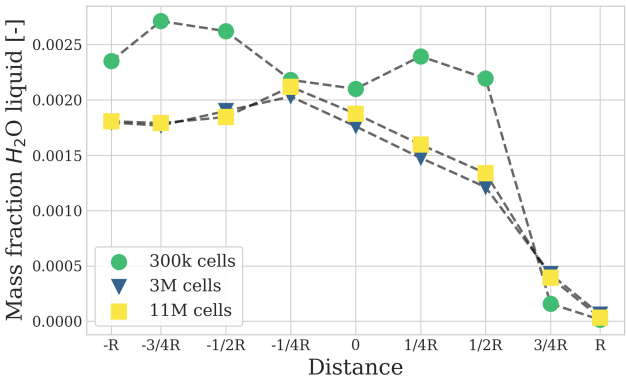

Figure 7: Profiles of condensed water mass fraction for different grid densities at vertical diameter of high-mixing junction outlet at the operating point P1wet.

3.2. Setup and condensation submodel

The segregated solver of STAR-CCM+ [37] is selected, employing second-order upwind discretization schemes for convective terms. Reynolds numbers of $18 \cdot 10^3$ and $51 \cdot 10^3$ are obtained for the inlet and EGR, respectively, which leads to the usage of either steady Reynolds-Average Navier-Stokes (RANS) or unsteady (URANS) turbulence approach, depending on the junction geometry. Turbulence closure has been obtained by means of the eddy-viscosity Shear Stress Transport (SST) $k-\omega$ model [38], which combines the formulation of Wilcox $k-\omega$ [39] model in the vicinity of the walls with the $k-\epsilon$ model in the free-stream region. The model calculates the turbulent viscosity as defined in Eq. 1

$$\mu_t = \rho k \mathcal{T} \tag{1}$$

by considering two transport equations: one corresponding to the turbulence kinetic energy k (Eq. 2) and another for the specific rate of dissipation ω (Eq. 3)[1]. For more details of the particular implementation of this turbulence model in STAR-CCM+, please refer to its user guide [37].

$$\frac{\partial}{\partial t}(\rho k)+\nabla\cdot(\rho k\overline{\mathbf{u}}) = \nabla\cdot[(\mu+\sigma_k\mu_t)\nabla k]+P_k-\rho\beta^* f_{\beta^*}(\omega k-\omega_{amb}k_{amb}) \tag{2}$$

[1]Please notice that ω affects μ_t through the calculation of the turbulent time scale $\mathcal{T}$.

$$\frac{\partial}{\partial t}(\rho\omega)+\nabla\cdot(\rho\omega\overline{\mathbf{u}}) = \nabla\cdot[(\mu+\sigma_\omega\mu_t)\nabla\omega]+ P_\omega-\rho\beta f_\beta\left(\omega^2-\omega_{amb}^2\right) \tag{3}$$

Steady RANS simulations are employed for the geometry shown in Fig. 5b, due to is low mixing, which keeps the fluctuation of the condensation MFR once converged below 1%. However, the geometry depicted in Fig. 5a required URANS due to the significant condensation oscillation produced by the detachment of the EGR stream when being injected into the inlet stream. The effect of such secondary flows on the transient behavior of the flow field has been analyzed by Galindo et al. [30]. The sensitivity of condensation prediction to time-step size has been assessed also at point P1wet (see Table 3) with the high-mixing junction (Fig. 5a), considering three different time-step sizes: $\Delta t = 10^{-4}$ s, $\Delta t = 5 \cdot 10^{-5}$ s and $\Delta t = 10^{-5}$ s. Condensation mass flow rate changes only by 0.01 % when comparing simulations with $\Delta t = 10^{-5}$ s and $\Delta t = 5 \cdot 10^{-5}$ s. A further coarsening on the time-step size from $\Delta t = 5 \cdot 10^{-5}$ to $\Delta t = 10^{-4}$ still provides a small variation of 0.09 % on condensed water. With these results, a time-step size of $\Delta t = 10^{-4}$ s is selected for the unsteady cases with a second-order implicit unsteady solver, which is similar to the one employed in the work of Galindo et al. [31] ($\Delta t = 2 \cdot 10^{-4}$ s). When unsteady simulations are employed, the solution is averaged for at least 40 ms, starting when condensation achieves a periodic state.

Regarding the boundary conditions, the mass flow rates, total temperatures and mass fraction of dry air and water vapor are set at both inlets (EGR and fresh air) in accordance with the corresponding working point (see section 4.2). A pressure boundary condition is employed at the outlet, whose value corresponds to the pressure of the test rig. Adiabatic walls are employed, considering the low thermal conductivity of the junctions material.

The condensation submodel corresponds to the one developed by Serrano et al. [29], which predicts the liquid condensation produced when two streams with different psychrometric conditions (temperature, pressure and specific humidity) are

mixed. This model estimates the generation of condensates in each cell that leads, through an isenthalpic process, to an equilibrium state at saturated conditions employing Dalton's Law and Antoine's equation for the saturation curve. The condensation submodel does not require additional boundary conditions to those mentioned in the previous paragraph; as it affects the simulation by modifying the transport equations implemented in STAR-CCM+ [37] through the source terms, which are presented in Eqs. 4, 5 and 6.

$$S_{vap} = \frac{\rho \gamma_{air}(w_f - w_1)}{\Delta t} \tag{4}$$

$$S_{ener.} = -S_{vap}(L - c_p T) \tag{5}$$

$$S_{mom..} = S_{vap}\overrightarrow{u} \tag{6}$$

A detailed description of the condensation submodel is provided by Serrano et al. [29], but the following underlying simplifications are highlighted:

- The model considers instantaneous condensation due to the low flow velocities existing at LP-EGR junctions and similar mixing applications. In these cases, it is acceptable to assume that condensation occurs instantaneously whenever a cell presents oversaturation.
- The distortion that condensed liquid water droplets may cause on the gaseous flow field is not modeled, since liquid water mass fraction is low.

The condensation submodel employed in this work presents a negligible increase of the computational cost compared to another alternatives for multiphase flow modeling, like employing Eulerian-Lagrangian approaches featuring droplet nucleation, growth and condensation models [40, 41].

4. Indirect measurement of condensation

The method to characterize the condensation mass flow rate indirectly through temperature measurements is derived in 4.1. Then, the operating conditions that have been measured (and subsequently simulated with 3D CFD) are indicated in 4.2. Finally, the steps to apply the proposed method to a certain working point are indicated in 4.3.

4.1. Derivation of method

The underlying idea of the proposed method is that the condensation due to the mixing of humid streams releases its latent heat, thus increasing the temperature of the flow. If the streams to be mixed were dry instead, condensation will not appear. Therefore, by comparing the temperature when condensation appears against that of the case without condensation with the same inlet conditions, one is able to quantify the condensation mass flow rate. In this way, the temperature is experimentally characterized at the section of interest (see Fig. 3) twice for the same working point: once injecting the desired water and again with no water injected. By casting the corresponding energy balances for the two configurations and assuming certain simplifications, it will be shown that the difference in temperature of the dry and humid cases is proportional to the released energy of the condensation process and, in turn, to the condensation mass flow rate.

Figure 8 shows a scheme of the volume control for the three-way junction, where the factors to take into account for the energy balance are presented. Equation 7 presents the energy balance in steady state, being $\dot{H}_0$ the flow rate of stagnation enthalpy associated to each stream, considering perfect gas assumption and averaging over the cross section (Eq. 8).

$$\dot{H}_{0\_in,air} + \dot{H}_{0\_in,EGR} + \dot{Q}_{cond} = \dot{H}_{0\_outlet} + \dot{Q}_{ext} \quad , where \tag{7}$$

$$\dot{H}_0 = \int_{SC} \rho \cdot \left(h + \frac{c^2}{2}\right) \cdot \overrightarrow{u} \cdot \overrightarrow{dA} = \dot{m} \cdot \overline{h_0} \overset{Assuming\ perfect,gas}{=} \dot{m} \cdot \overline{C_p} \cdot \overline{T_0} \tag{8}$$

Left hand side of equation 7 shows the enthalpies of the two inlet streams flowing into the three-way junction, being the (fresh air) inlet $\dot{H}_{0\_in,air}$ and the stream coming from the LP-EGR $\dot{H}_{0\_in,EGR}$. Another term on equation 7 is the heat released

due to condensation, which only appears in the test in which the water injection exists ($\dot{Q}_{cond}$). In the right hand side of equation 7, the enthalpy of the outlet flow (characterized by the thermocouple array) is $\dot{H}_{0\_outlet}$, and, finally, the term related to the heat exchanged with the surroundings is $\dot{Q}_{ext}$.

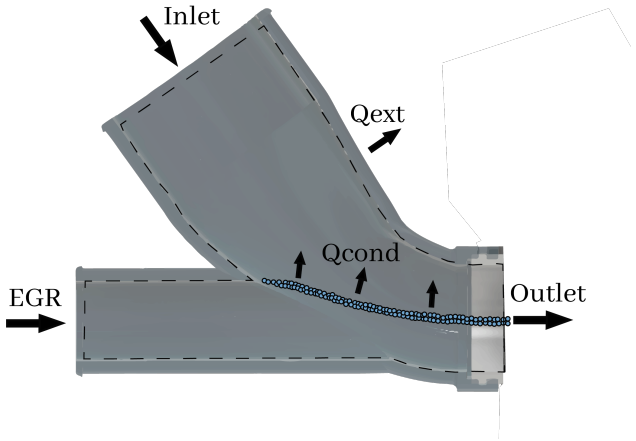

Figure 8: Scheme of control volume with energy transfers for a three-way junction with in-flow condensation.

Eq. 9 and Eq. 10 present the enthalpy balance for the cases with (w) and without (w/o) injection, respectively. In these, Eq. 7 is written for the considered case, isolating the stagnation outlet enthalpy. Equation 8 is used as well and $\dot{Q}_{cond}$ is expressed in terms of the latent heat L and the condensed mass flow rate of water $\dot{m}_{H_2O}$.

$$\left[\dot{m}_t \cdot \overline{cp} \cdot \overline{T}_{0,out}\right]_w = \dot{m}_{H_2O} \cdot L - \dot{Q}_{ext,w} + \left[\dot{m}_{in} \cdot \overline{cp}_{in} \cdot T_{0,in}\right]_w + \left[\dot{m}_{EGR} \cdot \overline{cp}_{EGR} \cdot T_{0,EGR}\right]_w \quad (9)$$

$$\left[\dot{m}_t \cdot \overline{cp} \cdot \overline{T}_{0,out}\right]_{w/o} = 0 - \dot{Q}_{ext,w/o} + \left[\dot{m}_{in} \cdot \overline{cp}_{in} \cdot T_{0,in}\right]_{w/o} + \left[\dot{m}_{EGR} \cdot \overline{cp}_{EGR} \cdot T_{0,EGR}\right]_{w/o} \quad (10)$$

Equation 11 considers the subtraction between Eq. 10 and 9, assuming that the heat transfer with the surroundings is the same for both cases ($Q_{ext,w} = Q_{ext,w/o}$):

$$\dot{m}_t \cdot \overline{cp} \cdot \overline{T_{0,out,w/o}} = \dot{m}_t \cdot \overline{cp} \cdot \overline{T_{0,out,w}} - \dot{m}_{H_2O} \cdot L \quad (11)$$

Equation 12 then presents the calculation of the water mass flow rate condensed by the the mixing of two streams for each area division (see section 2.2), considering that the mass flow rate is evenly distributed. Finally, Equation 13 provides the total condensation mass flow rate going through the junction outlet.

$$\dot{m}_{H_2O}(i) = \frac{\frac{\dot{m}_t}{N} \cdot \overline{cp}(i) \cdot \left(\overline{T_{0,out,w}}(i) - \overline{T_{0,out,w/o}}(i)\right)}{L} \quad (12)$$

$$\dot{m}_{H_2O} = \sum_{i=1}^{N=97} \dot{m}_{H_2O}(i) \quad (13)$$

A non-comprehensive list of the explicit and implicit hypotheses assumed for the indirect measurement of condensation flow rates would include: considering that introducing humidity on EGR stream and condensation does not affect neither the velocity flow field nor heat transfer with the surroundings, neglecting the effect of gravity over the condensed droplets, so that they are convected by the flow in the same way as the released heat, and assuming a homogeneous distribution of mass flow rate at the target cross-section.

4.2. Test campaign

In order to proceed with the indirect measurement of water mass fraction as shown in section 4.1, two different specific humidity conditions (wet and dry) need to be measured for each operating condition. A test matrix is proposed in Table 3 considering two different working points, where the inlet mass flow rates and EGR rates correspond to the operating range of a C-segment passenger car [15].

A higher EGR temperature than the dew conditions was set, in order to prevent condensation at the cooler (see Fig. 1) from happening [15] and therefore study the condensation generated only on the three-way junction. Finally, a low temperature (near 0°C) was set at the inlet, to represent intake from a cold ambient.

Regarding the three-way junction geometries (Fig. 5), two different designs are used to create variations on the mixing pattern than entail different temperature distributions. On the one hand, a low-mixing junction is depicted in Fig. 5b, in which the

Operating points	P1wet	P1dry	P2wet	P2dry
EGR Temperature [°C]	50	50	50	50
EGR Rate [%]	21	21	32	32
Specific Humidity [g/kg]	60	0	60	0
Inlet Temperature [°C]	-2	-2	0	0
Inlet mass flow [kg/h]	150	150	85	85

Table 3: Test Matrix

EGR branch is oriented in the same direction as the outlet duct. On the the other hand, Fig. 5a shows a high-mixing junction, whose design promotes homogenization by injecting the EGR facing the fresh air inlet. By considering two geometries and two operating conditions, the accuracy of the proposed technique and the validation of the 3D-CFD condensation model is assessed with different condensation patterns at the outlet cross section.

It is worth highlighting that three-way junction design determines the flow distribution at its outlet. In this way, a heterogeneous flow with low EGR and air mixing is related with reduced condensation [9], but the impact of flow heterogeneity on compressor performance has not a clear trend according to the current body of research [10, 42, 26, 27].

4.3. Example of application of proposed method

Figure 9 shows the different steps required to obtain the indirect measurement of condensation as proposed in Section 4.1, with an example of application. A custom postprocessing script is programmed in Python. A 500x500 grid is employed to linearly interpolate the scattered data coming from the 97 temperature samples (grey dots in Fig. 9). In this way, a continuous temperature field can be depicted at the junction outlet section, allowing to also calculate and display iso-contours as can be seen in Fig. 9.

Firstly, Figure 9a shows the temperature measurement for P1wet (with injection; see Table 3) at the cross section of study when the low-mixing junction Fig. 5b is used. In parallel, Figure 9b shows the temperature P1dry, where no injection is employed. Then, the difference of the temperature scalar field in the cross section between Fig. 9a and Fig. 9b is shown in Fig. 9c. In this picture, there is a region with no difference in temperature (hence, without condensation) and another region (the interface where the streams are mixed) where a positive temperature difference appears due to the local heat released as a consequence of condensation. Finally, Fig. 9d shows the water condensation at the outlet section when applying Eq. 12 to the difference in temperature shown in Fig. 9c.

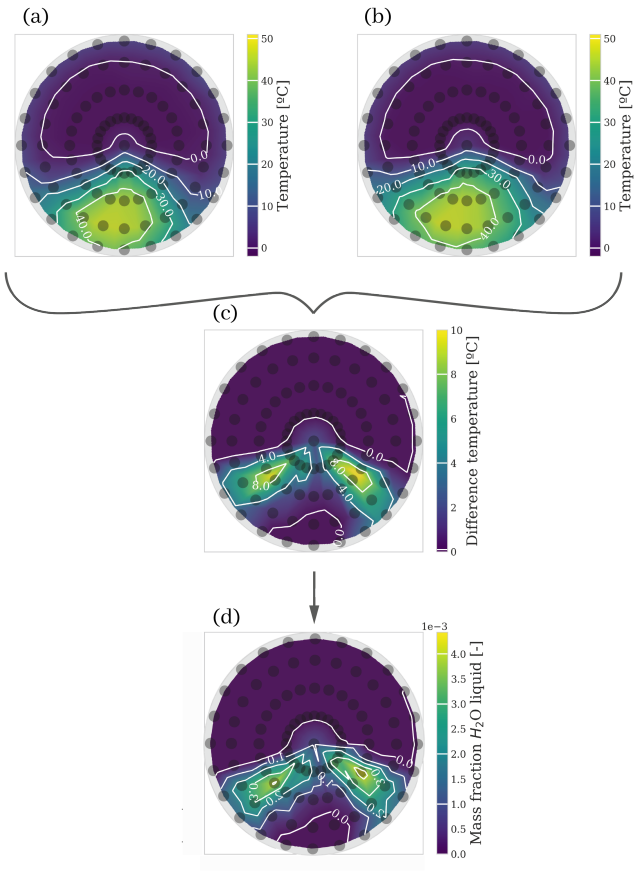

Figure 9: Temperature cross section at working points P1wet (a) and P1dry (b) with the temperature difference (c) between figure (a) and (b) and the water mass fraction obtained by the temperatures (d), corresponding to the low-mixing three-way junction.

5. Results and discussion

The results are divided in three sections. Firstly, the temperature distribution at the cross section is assessed in section 5.1. Then, the pattern of liquid water mass fraction produced by

condensation is shown in section 5.2. Finally, the total mass flow rate of condensed water going through the cross section is provided in section 5.3. In all the sections, experimental results are compared against CFD predictions for two junction designs (see Figure 5) and two operating conditions (see Table 3).

5.1. Temperature: CFD vs experiments

Temperature contours at the junction outlet cross section shown in Fig. 2, obtained by 3D-CFD simulations as well as measured experimentally, are shown in Fig. 10 (for the low-mixing junction) and Fig. 11 (for the high-mixing junction). Experimental data is gathered with the strategy described at Section 2.2 for the two operating points with water injection activated ("wet", in Table 3), so that there is condensation due to mixing. CFD results are obtained at the cross section mesh but then resampled at the 97 locations displayed in Fig. 3, for the sake of consistency with the experimental data.

Figures 10a and 10b show the temperature distribution at the working point P1wet when the low-mixing three-way junction is employed, for the experimental test and for the 3D-CFD simulation. As can be seen, a similar pattern is found with both methods: a higher temperature at the bottom of the section, representing the core of the EGR stream; a lower temperature at the upper part, corresponding to the cold fresh air and a strong temperature gradient located in the interface of both regions. The temperature field is consistent with the objective of the design of keeping the streams separated, i.e., with low mixing. The temperature gradient in the interface is steeper for the CFD case (Fig. 10b) than for the experiments (Fig. 10a).

Figures 10c and 10d depict temperature contours at the working point P2wet, again for the three-way junction that is designed to reduce the mixing between streams. Temperature distributions follow the same pattern as already described for Figs. 10a and 10b. In the case of point P2wet, the higher EGR rate compared to point P1wet (see Table 3) increases the hot area for both experimental and numerical results.

It is worth noting that CFD predictions of temperature (Fig. 10b and 10d) depict a maximum of 50 °C, corresponding to the inlet

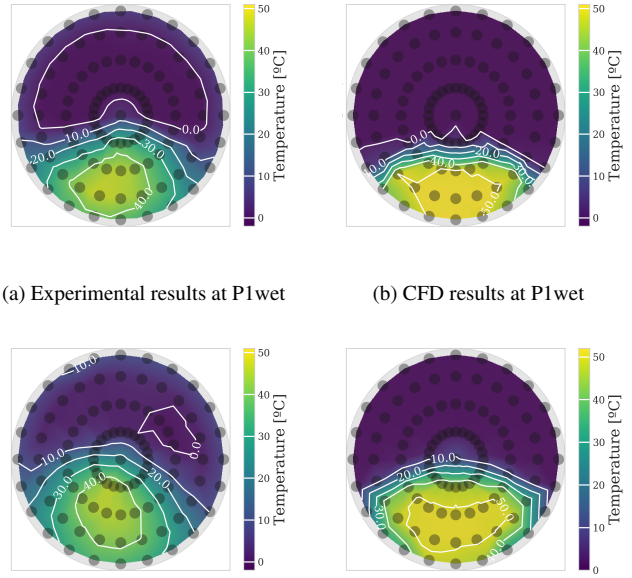

(a) Experimental results at P1wet

(b) CFD results at P1wet

(c) Experimental results at P2wet

(d) CFD results at P2wet

Figure 10: Temperature contours at low-mixing three-way junction outlet for two operating conditions, obtained by experiments and CFD simulations.

EGR temperature (see table 3). However, experimental measurements do not achieve the same temperature of 50 °C (see Fig. 10a and 10c) due to the heat transfer with the surroundings. Indeed, the minimum temperature of the experiments is about 0 °C (air inlet temperature in table 3), but it is achieved only at the core of the fresh air stream. Heat transfer is again responsible for this observed tendency of the fluid at the vicinity of the walls to present temperatures closer to the cross-section average in the experiments than what is predicted by CFD. In any case, the method developed in section 4 does not employ directly the values of the temperature at the humid working points P1wet and P2wet (Fig. 10a and 10c) but the temperature differences with their dry counterparts P1dry and P2dry. Therefore, the effect of neglecting the heat transfer in CFD should not be a major concern for the experimental indirect determination of the condensation mass fractions, provided that heat transfer remains the same with and without condensation, as assumed by Eq. 11.

Regarding the cases with the high-mixing three-way junction, Figures 11a and 11b show the temperature contours for

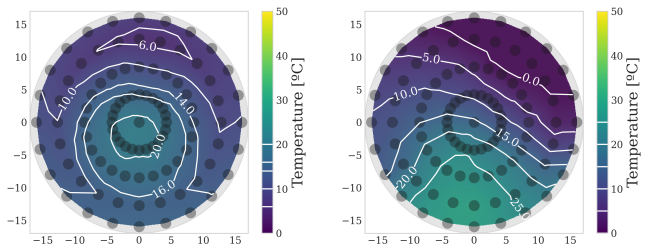

(a) Experimental results at P1wet

(b) CFD results at P1wet

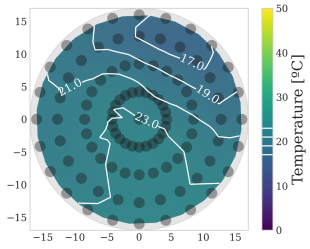

(c) Experimental results at P2wet

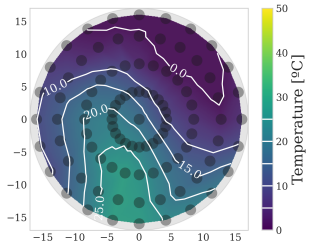

(d) CFD results at P2wet

Figure 11: Temperature contours at high-mixing three-way junction outlet for two operating conditions, obtained by experiments and CFD simulations.

operating conditions P1wet. The change in pattern compared to Fig. 10 is significant: while CFD simulations (Fig. 11b) predict the EGR stream to be still located at the bottom of the section but with a much gradual transition towards the cold region, the experiments (Fig. 11a) show that the EGR core with the high-mixing junction is able to penetrate the cold stream and be located at the middle of the cross section. In any case, both methods suggest at P1wet higher mixing in terms of lower temperature gradients than that of their counterparts with the low-mixing junction: Fig. 10a and Fig. 10b. When shifting to point P2wet, CFD (Fig. 11d) predicts a higher penetration of the EGR stream, whereas experiments (Fig. 11c) show the greatest flow homogeneity of all the cases, with a temperature range at the cross-section of only 6 °C. Fig. 11c and Fig. 11d show also at P2wet reduced temperature differences due to the enhanced mixing of the junction displayed in Fig. 5a when compared with the results provided by the low-mixing junction (Fig. 10c and Fig. 10d).

In order to quantify the difference between temperature distributions obtained experimentally and numerically (as displayed in Fig. 10 and Fig. 11), the root mean square error (RMSE) is defined as follows:

$$RMSE = \sqrt{\frac{\sum_{i=1}^{N=97} \left(T_{exp,i} - T_{CFD,i}\right)^2}{n}} \,. \tag{14}$$

Since the maximum temperature difference that could be observed is

$$\Delta T_{max} = T_{EGR} - T_{inlet} \,, \tag{15}$$

which can be calculated for each working point using the information from Table 3, it will be used to normalize $RMSE$ (Eq. 14) by means of the following expression:

$$\widetilde{RMSE} = \frac{RMSE}{\Delta T_{max}} \cdot 100 \,. \tag{16}$$

Table 4 presents the results of $\widetilde{RMSE}$ for all the studied cases. As can be seen, the error between techniques is small, with $\widetilde{RMSE}$ of temperature distributions ranging between 2.8 % and 4.4 %. In this way, the CFD model is regarded as appropriate to predict the experimental temperature distributions. It is worth mentioning that the experiment may present some features that are not modeled and would have an impact on junction outlet temperature distribution, including: non-homogeneous velocity and temperature distribution at the junction inlets (despite the long, straight ducts), three-way junction manufacturing imperfections, junction conductive heat transfer and external convective heat transfer (despite material low conductivity).

Operating point	Junction	$\widetilde{RMSE}$ [%]
P1wet	Low-mixing	2.81
P1wet	High-mixing	2.76
P2wet	Low-mixing	4.39
P2wet	High-mixing	3.72

Table 4: Normalized RMSE for each working point and junction geometry.

5.2. *Condensation mass fraction: CFD vs experiments*

Contours of condensed liquid water mass fraction at the outlet cross section are displayed in Fig. 12 and Fig. 13, considering the low-mixing and high-mixing junctions, respectively.

Experimental results have been obtained with the method developed in this work, explained in section 4. The condensation submodel described in section 3.2 and embedded in the 3D CFD cases is the one responsible for providing the numerical results. Again, CFD results have been resampled at the experimental thermocouple locations (see Fig. 3).

Figure 12 shows how the low-mixing junction prevents condensation from happening outside the air-EGR interface discussed in Fig. 10, which means that both the cold and hot streams present an unmixed core and only interact through that interface. Besides, it also confirms the shift of the interface towards the upper part of the cross section when increasing the EGR rate from P1wet to P2wet operating conditions, both for the experimental (Figs. 12a and 12c) and numerical (Figs. 12b and 12d) methods. The existence of condensation only at the air-EGR interface for the low-mixing junction and the modification of the location of such interface with the working point was also observed experimentally by Galindo et al. [30] with their planar laser-induced visualization of droplet patterns. In this way, Fig. 12 shows that there is a strong agreement between the CFD predictions and the indirect measurements of condensation for the low-mixing junction.

The much wider regions with non-zero condensation mass fraction displayed in Fig. 13 for the high-mixing junction, compared to those of the low-mixing junction (Fig. 12), establish a clear relation between junction design, mixing between streams and subsequent formation of condensation. Only the measurements for P1wet (Fig. 13a) suggest that the EGR stream has penetrated into the cold stream and there is an outer area surrounding that jet (see Fig. 11a), almost free from condensation. The rest of cases of Fig. 13 show generalized mixing and condensation. Planar laser-induced visualization of condensation [30] for the high-mixing junction also provide patterns with fog across the whole section, showing less intensity at the upper part as depicted in Fig. 13.

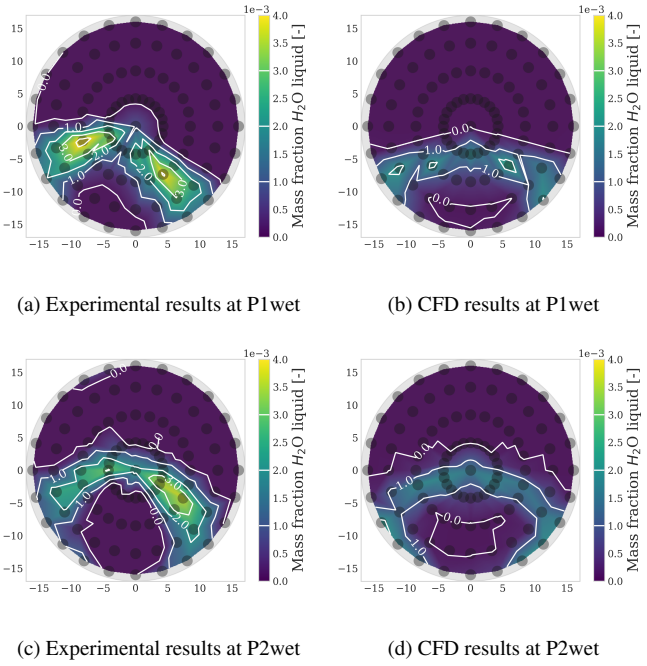

(a) Experimental results at P1wet (b) CFD results at P1wet

(c) Experimental results at P2wet (d) CFD results at P2wet

Figure 12: Condensation mass fraction contours at low-mixing three-way junction outlet for two operating conditions, obtained by experiments and CFD simulations.

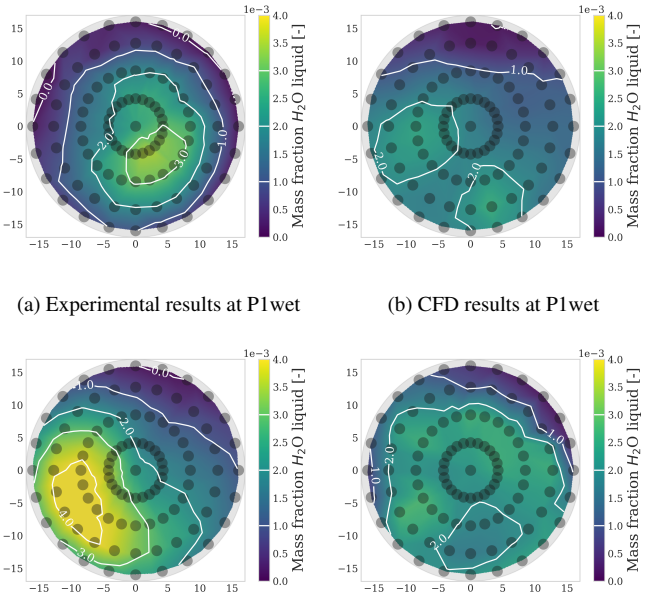

(a) Experimental results at P1wet (b) CFD results at P1wet

(c) Experimental results at P2wet (d) CFD results at P2wet

Figure 13: Condensation mass fraction contours at high-mixing three-way junction outlet for two operating conditions, obtained by experiments and CFD simulations.

5.3. Condensation mass flow rate: CFD vs experiments

In order to conduct a quantitative comparison of the condensed mass flow rate through the junction outlet cross section between experiments and CFD simulations, it is normalized with the total mass flow rate leaving the junction. Equation 17 shows the average mass fraction of liquid water obtained in this way:

$$\overline{\gamma_{cond}} = \frac{\dot{m}_{H_2O}}{\dot{m}_{tot,out}} \tag{17}$$

Besides, Eq. 18 computes a relative difference between average mass fractions of condensed water, considering the corresponding experimental and CFD results for each case:

$$\varepsilon = \frac{\left|\overline{\gamma_{cond}}_{,CFD} - \overline{\gamma_{cond}}_{,exp}\right|}{\overline{\gamma_{cond}}_{,exp}} \cdot 100 \tag{18}$$

Figure 14 shows the comparison between the average mass fraction of condensed water calculated with Eq. 17, at the high-mixing and low-mixing junctions (see Fig. 5) for the operating conditions P1wet and P2wet (see table 3). The average mass fractions are obtained experimentally and numerically, and the relative difference between them (Eq. 18) is displayed. Figure 14 shows the great increase of condensation when replacing the low-mixing with the high-mixing junction, as was anticipated when Fig. 12 and Fig. 13 were compared. Besides, while shifting from P1wet to P2wet (and thus increasing the EGR rate) with the low-mixing junction does not change significantly the condensation mass flow rate, it does magnify the average mass fraction of liquid water for the high-mixing junction.

Finally, the relative differences depicted in Fig. 14 range between 2 and 27%. A weighted-average error of $\bar{\varepsilon} = 11\%$ is calculated using Eq. 19. The fair agreement between CFD simulations and experimental measurements allow the trends to be consistent for each operating point and geometry regardless of the method, as shown in Fig. 14.

$$\bar{\varepsilon} = \frac{\sum_i \left|\dot{m}_{H_2O,CFD} - \dot{m}_{H_2O,exp}\right|}{\sum_i \dot{m}_{tot,out}} \cdot 100 \tag{19}$$

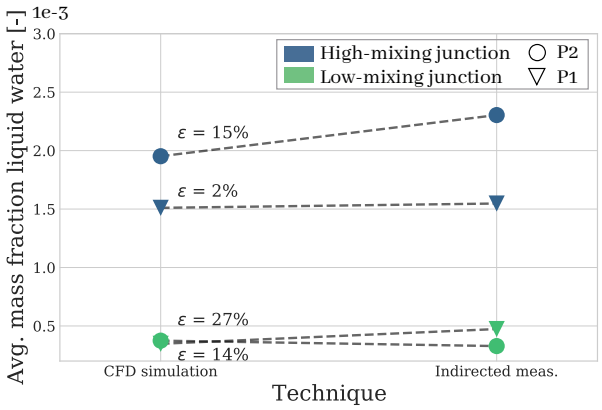

Figure 14: Average mass fraction of liquid water for two junctions at two operating conditions, with relative differences between measurements and simulations.

6. Concluding remarks

In this work, a novel technique to experimentally characterize the in-flow condensation patterns and mass flow rate has been developed. A humid gas stand is employed to produce bulk condensation due to flow mixing in a three-way junction. To the author's knowledge, condensation mass fractions have been measured (indirectly) for the first time. Experimental condensation patterns are obtained by comparing temperature distributions with or without humidity and combining the corresponding enthalpy balances. Besides, these results are compared with RANS and URANS CFD simulations featuring an embedded condensation submodel [29], for two working points and two junction designs.

The experimental temperature distributions are challenging to be predicted by CFD at certain conditions, in which transient features such as flow detachments can be observed. In such cases, simulations with scale-resolving turbulence models should provide predictions with higher fidelity than those obtained by RANS and URANS [18], as employed in this work. Besides, modeling heat transfer with the surroundings may improve the accuracy of the thermal flow field and subsequent condensation. Nevertheless, all CFD cases presented normalized RMSE for the temperature distributions below 5%. With this, the 3D CFD models is known to predict accurately not only

temperature distributions but also secondary flows and qualitative condensation patterns [30].

Indirect condensation measurements and CFD predictions are in good agreement in terms of condensation mass flow rates and trends, with an average difference of 11%. In this case, condensation measurements cannot be considered as a reference of accuracy by themselves, since they have been obtained indirectly with a developed method that employs certain hypotheses. Considering the consistency between condensation results obtained experimentally and numerically, the feasibility of the indirect measurement hypotheses (see end of Section 4.1) and the aforementioned predicting abilities of the 3D CFD model, the conclusion of this work is twofold: the developed experimental method is useful to measure indirectly condensation flow rate patterns, and the in-flow condensation submodel developed by Serrano et al. [29] is quantitatively validated. Both approaches can be used by researchers to determine the condensation risk at different operating conditions. Galindo et al. [31] already linked the existence of higher condensation rates with greater impeller wear for the case of LP-EGR applications. Besides, the validated 3D CFD model and the experimental method can be employed as a tool to improve junction designs. Indeed, the paper has shown the great importance of the three-way junction geometry. A careful design can prevent mixing between streams from happening, limiting the interaction to a thin interface and thus reducing significantly condensation.

7. Acknowledgements

The authors of this paper wish to thank Alejandro Hernández Salmerón and David González Domínguez for his invaluable support during the laboratory setup and the experimental campaign. Francisco Moya is partially supported through a FPI-GVA-ACIF-2019 grant of the Government of Generalitat Valenciana and the European Social Fund. This work has been partially supported by "Conselleria de Innovación, Universidades, Ciencia y Sociedad Digital de la Generalitat Valenciana" through grant number GV/2020/008.

List of Symbols

A	Area	m^2
β, β^*	SST $k-\omega$ model coefficients	–
c	Absolute velocity	$m \cdot s^{-1}$
c_p	isobaric specific heat capacity	$J \cdot kg^{-1} \cdot K^{-1}$
Δt	time-step size	s
f_β^*	free-shear modification factor	–
f_β	vortex-stretching modification factor	–
γ	mass fraction	–
H	enthalpy	$J \cdot s^{-1}$
k	turbulent kinetic energy	$m^2 \cdot s^{-2}$
L	latent heat	$J \cdot kg^{-1}$
$\dot{m}$	mass flow rate	$kg \cdot s^{-1}$
N	Number of temperature probe locations at junction outlet	–
$\dot{Q}$	Heat transfer	$J \cdot s^{-1}$
P_k	Production term (k)	$kg \cdot m^{-1} \cdot s^{-3}$
P_w	Production term (w)	$kg \cdot m^{-3} \cdot s^{-2}$
S	Source Term	

List of Symbols (cont.)

σ_k, σ_ω	SST $k-\omega$ model coefficients	–
t	time	s
T	temperature	K
U	characteristic velocity	$m \cdot s^{-1}$
$\vec{u}$	velocity	$m \cdot s^{-1}$
w	specific humidity	$g_{H_2O} \cdot kg_{air}^{-1}$
x	coordinate in dominant direction	m
ϵ_R	relative error	%
μ	dynamic viscosity	$kg \cdot m^{-1} \cdot s^{-1}$
μ_t	turbulent eddy viscosity	$kg \cdot m^{-1} \cdot s^{-1}$
ρ	density	$kg \cdot m^{-3}$
ω	Specific rate of dissipation	$1 \cdot s^{-1}$
$\mathcal{T}$	turbulent time scale	s

References

[1] L. Yang, J. Wang, Y. Jiang, L. Zou, Oil water flow splitting in eccentric annular T-junction tubes Experimental and CFD analysis, Chemical Engi-

Sub- and Superscripts

0	stagnation variable
air	air flow
amb	ambient turbulence values that counteract turbulence decay
cells	cells at the mesh
cond	condensates
dry	Case with water injection
EGR	egr flow
ener.	energy
ext	external
H_2O	liquid water
i	data for each time step
in	intake flow
mom.	momentum
outlet	outlet flow
sat	saturation
t	total including inlet and EGR
w	Test with water injection
w/o	Test without water injection
vap	water vapor
water	liquid water
wet	Case with water injection

List of abbreviations

EGR	Exhaust gas recirculation
LP-EGR	Low-pressure EGR
MFR	Mass flow rate
NOx	Nitrogen oxides
RANS	Reynolds-Averaged Navier-Stokes
RMSE	Root mean square error
SST	Shear Stress Transport
URANS	Unsteady RANS

neering Science 228 (2020) 1–13. doi:10.1016/j.ces.2020.116000.

[2] T. Lu, D. Attinger, S. M. Liu, Large-eddy simulations of velocity and temperature fluctuations in hot and cold fluids mixing in a tee junction with an upstream straicht or elbow main pipe, Nuclear Engineering and Design 263 (2013) 32–41. doi:10.1016/j.nucengdes.2013.04.002.

[3] B. Yang, W. Su, S. Deng, L. Zhao, P. Lu, State-of-art of impacting T-junction : Phase separation, constituent separation and applications, International Journal of Heat and Mass Transfer 148 (2020) 1–10. doi:10.1016/j.ijheatmasstransfer.2019.119067.

[4] L. Vyskocil, J. Schmid, J. Macek, CFD simulation of air–steam flow with condensation, Nuclear Engineering and Design 279 (2014) 147–157. doi:10.1016/j.nucengdes.2014.02.014.

[5] S. Reifarth, E. Kristensson, J. Borggren, A. Sakowitz, H.-E. Angstrom, Analysis of EGR/Air Mixing by 1-D Simulation, 3-D Simulation and Experiments, Tech. rep., SAE Technical Paper (2014). doi:10.4271/2014-01-2647.

[6] J. Galindo, H. Climent, R. Navarro, J. Miguel-García, A study on the high pressure EGR transport and application to the dispersion among cylinders in automotive engines, International Journal of Engine Research (2020). doi:10.1177/1468087420969263.

[7] N. Zheng, L. Zhao, J. Wei, Experimental research on liquid-vapor two-phase flow separation of zeotropic mixtures at an impacting T-junction 89 140–152. doi:10.1016/j.expthermflusci.2017.08.012.

[8] P. Vojkuvkova, O. Sikula, J. Weyr, Assessment of condensation of water vapor in the mixing chamber by CFD method, in: EPJ Web of Conferences, Vol. 92. doi:10.1051/epjconf/20159202112.

[9] J. Galindo, R. Navarro, D. Tarí, G. García-Olivas, Centrifugal compressor influence on condensation due to Long Route-Exhaust Gas Recirculation mixing, Applied Thermal Engineering (2018). doi:10.1016/j.applthermaleng.2018.09.005.

[10] S. Guilain, R. Boubennec, M. Doublet, C. Clement, R. Navarro, D. Tarí, F. Moya, Condensation before compressor: a key issue of Low Pressure EGR in Eu7 context, in: 24th Supercharging Conference 2019, 2019.

[11] A. Castorrini, A. Corsini, F. Rispoli, P. Venturini, K. Takizawa, T. E. Tezduyar, Computational analysis of wind-turbine blade rain erosion, Computers & Fluids 141 (Supplement C) (2016) 175 – 183. doi:10.1016/j.compfluid.2016.08.013.

[12] P. Z. John, T. Koka, S. Dayalan, Water droplet erosion simulation of a turbocharger compressor wheel, in: ASME Turbo Expo 2014: Turbine Technical Conference and Exposition, no. GT2014-26974, American Society of Mechanical Engineers, 2014.

[13] P. Michel, A. Charlet, G. Colin, Y. Chamaillard, G. Bloch, C. Nouillant, Optimizing fuel consumption and pollutant emissions of gasoline-HEV with catalytic converter, Control Engineering Practice 61 (2017) 198 – 205. doi:10.1016/j.conengprac.2015.12.010.

[14] J. Galindo, V. Dolz, J. Monsalve-Serrano, M. Maldonado, L. Odillard, Advantages of using a cooler bypass in the low-pressurre exhaust gas recirculation line of a compression ignition diesel engine operating at cold conditions, Internal Journal of Engine Research (2020). doi:10.1177/1468087420914725.

[15] J. Galindo, R. Navarro, D. Tari, F. Moya, Development of an experimental test bench and a psychrometric model for assessing condensation on a Low Pressure EGR cooler, International Journal of Engine Research 22 (2020) 1540–1550. doi:10.1177/1468087420909735.

[16] K. L. Wang, D. Li, N. Husnain, S. Fareed, Numerical and experimental investigation on water vapor condensation in turbulent flue gas, Applied Thermal Engineering 160 (2019). doi:10.1016/j.applthermaleng.2019.114009.

[17] M. Georgiou, M. V. Papalexandris, Turbulent mixing in T-junctions: The role of the temperature as an active scalar, International Journal of Heat and Mass Transfer 115 (2017) 793–809. doi:10.1016/j.ijheatmasstransfer.2017.08.081.

[18] A. Sakowitz, M. Mihaescu, L. Fuchs, Turbulent flow mechanisms in mixing T-junctions by Large Eddy Simulations, International Journal of Heat and Fluid Flow 45 (2014) 135–146. doi:10.1016/j.ijheatfluidflow.2013.06.014.

[19] C. Evrim, X. Chu, E. Laurien, Analysis of thermal mixing characteristics in different T-junction configurations, International Journal of Heat and Mass Transfer 158 (2020) 1–10. doi:10.1016/j.ijheatmasstransfer.2020.120019.

[20] C. Evrim, E. Laurien, Numerical study of thermal mixing mechanisms in T-junctions, Applied Thermal Engineering 138 (2021) 1–13. doi:10.1016/j.applthermaleng.2020.116155.

[21] C. Evrim, E. Laurien, Large-Eddy Simulation of turbulent thermal flow mixing in a vertical T-junction configuration, International Journal of Thermal Sciences 150 (2020) 1–12. doi:10.1016/j.ijthermalsci.2019.106231.

[22] M. Zhou, R. Kulenovic, E. Laurien, Advanced flow pattern for describing tangential flow oscillation in thermal-mixing pipe flow at a horizontal T-Junction, International Journal of Thermal Sciences 136 (2019) 328–336. doi:10.1016/j.ijthermalsci.2018.10.045.

[23] M. Zhou, R. Kulenovic, E. Laurien, T-junction experiments to investigate thermal-mixing pipe flow with combined measurement techniques, Applied Thermal Engineering 150 (2019) 237–249. doi:10.1016/j.applthermaleng.2018.12.161.

[24] A. Bornschlegell, J. Pelle, S. Harmand, A. Bekrar, Thermal optimization of a single inlet T-junction, International Journal of Thermal Sciences 53 (2012) 108–118. doi:10.1016/j.ijthermalsci.2011.09.016.

[25] K. H. Brune, H. P. Schiffer, R. Christmann, M. Gnewikow, Experimental Investigations of the Disturbed Inlet-Flow Structure Caused by Mixing Geometries and Its Influence on the Performance of a Turbocharger Centrifugal Compressor, ASME Turbo Expo (2009) 1295–1304doi:10.1115/GT2009-59534.

[26] A. Reihani, J. Hoard, S. Klinkert, C.-K. Kuan, D. Styles, Numerical Evaluation of the Effects of Low Pressure EGR Mixer Configuration on Turbocharger Compressor Performance, in: ASME 2018 Internal Combustion Engine Division Fall Technical Conference, American Society of Mechanical Engineers Digital Collection, 2018.

[27] A. Reihani, J. Hoard, S. Klinkert, C.-K. Kuan, D. Styles, G. McConville, Experimental response surface study of the effects of low-pressure exhaust gas recirculation mixing on turbocharger compressor performance, Applied Energy 261 (2020) 114349. doi:10.1016/j.apenergy.2019.114349.

[28] B. Yang, W. Su, S. Deng, L. Zhao, State-of-art of branching T-junction: Experiments, modeling, developing prospects and applications, Experimental Thermal and Fluid Sciences 109 (2019). doi:10.1016/j.expthermflusci.2019.109895.

[29] J. Serrano, P. Piqueras, R. Navarro, D. Tarí, C. Meano, Development and verification of an in-flow water condensation model for 3D-CFD simulations of humid air streams mixing, Computers & Fluids 167 (2018) 158 – 165. doi:10.1016/j.compfluid.2018.02.032.

[30] J. Galindo, R. Navarro, D. Tari, F. Moya, Analysis of condensation and secondary flows at T-junctions using optical visualization techniques and Computational Fluid Dynamics, International Journal of Multiphase Flow (2021). doi:10.1016/j.ijmultiphaseflow.2021.103674.

[31] J. Galindo, P. Piqueras, R. Navarro, D. Tarí, C. M. Meano, Validation and sensitivity analysis of an in-flow water condensation model for 3D-CFD simulations of humid air streams mixing, International Journal of Thermal Sciences 136 (2018) 410–419. doi:10.1016/j.ijthermalsci.2018.10.043.

[32] Z. Wang, S. Sanders, J. A. Backhaus, A. Munnannur, N. M. Schmidt, H2O absorption tomography in a diesel aftertreatment system using a polymer film for optical access, Applied Physic B 127 (2017). doi:10.1007/s00340-017-6867-8.

[33] J. Choi, S. Satpathy, J. Hoard, D. Styles, C. Kuan, An Experimental and Computational Analysis of Water Condensation Separator Within a Charge Air Cooler, International Combustion Engine Division Fall Technical Conference (2017) 1–11doi:10.1115/ICEF2017-3609.

[34] E. Randolph, F. Bocher, S. Kroll, N. Wright, Visual, Thermodynamic, and Electrochemical Analysis of Condensate in a Stoichiometric Spark-Ignited EGR Engine, SAE Technical Paper (2017) 1–12doi:10.4271/2018-01-1406.

[35] L. Chen, X. Zhang, C. Wang, C. Yang, Analysis on High-Pressure Water Separator, Procedia Engineering 121 (2015) 558–566. doi:10.1016/j.proeng.2015.08.1034.

[36] E. Randolph, F. Bocher, S. Kroll, N. Wright, Research and development of Self-contained Water Injection Systems, International Journal of Environmental Research and Public Health 18 (2017) 1–10. doi:10.3390/ijerph18105392.

[37] CD-adapco, STAR-CCM+, release version 12.06.010 Edition (February 2018).
URL http://ww.cd-adapco.com

[38] F. R. Menter, Two-equation eddy-viscosity turbulence models for engineering applications, AIAA journal 32 (8) (1994) 1598–1605. doi:10.2514/3.12149.

[39] D. C. Wilcox, Reassessment of the scale-determining equation for advanced turbulence models, AIAA journal 26 (11) (1988) 1299–1310. doi:10.2514/3.10041.

[40] T. Wittmann, C. Bode, J. Friedrichs, The Feasibility of an Euler-Lagrange Approach for the Modeling of Wet Steam, Journal of Engineering for gas

turbines and power 143 (2021) 1–8. doi:10.1115/1.4049859.

[41] T. Wittman, S. Luck, C. Bode, J. Friedrichs, Numerical Simulation of Nucleation and Condensation and Radial Turbines, in: CAD-FEM ANSYS Simulation Conference, Dusseldorf, Germany, 2019.

[42] J. Galindo, J. R. Serrano, R. Navarro, G. García-Olivas, Numerical modeling of centrifugal compressors with heterogeneous incoming flow due to Low Pressure exhaust gas recirculation, in: Proceedings of ASME Turbo Expo 2020. doi:10.1115/GT2020-16030.